2007 IEEE International Conference on
Robotics and Automation
Roma, Italy, 10-14 April 2007

Development of a Flying Robot with Pantograph-based Variable Wing Mechanism

Naohiro Hara, Kazuo Tanaka, Hiroshi Ohtake and Hua O. Wang

Abstract— **We develop a flying robot with a new pantograph-based variable wing mechanism for horizontal-axis rotorcrafts (cyclogyro rotorcrafts). A key feature of the new mechanism is a unique trajectory of variable wings that not only change angles of attack but also expand and contract according to wing positions. Experimental results show that the developed flying robot can generate 144% lift force for its own weight (equivalently 100 gf payload). Furthermore, as a result of optimizing design parameters of the robot through computer simulation, we arrive at the optimal design parameters with 200 gf payload. Both simulation and experimental results show the utility of the developed flying robot with the new mechanism.**

I. Introduction

There have been a number of studies on flying machines in the last few decades. A lot of studies on airplanes and gliders as fixed wing aircrafts, helicopters as vertical-axis rotorcrafts, and balloons as lighter-than-air aircrafts have focused on improving the flying performance rather than on developing a new and innovative flying mechanism.

In recent years, flying robotics researches [1] [2] [3] have been conducted from the biologically inspired points of view. Most of the studies focuses on developing a new flying mechanism. Another interesting topic on flying robots is micro air vehicles (MAVs). In particular, the DARPA project (e.g., [4], [5]) on MAVs is well known.

Very recently, a new and innovative mechanism [6] [7] [8] for very few types of horizontal-axis rotorcrafts has been proposed. The horizontal-axis rotorcrafts are called "cyclogyro" [9]. Cyclogyro that is a unique mechanism of generating lift forces was proposed in 1930's. An aeroplane with the mechanism was designed at the time. The cyclogyro is an aeroplane propelled and given lift by horizontal assemblies of rotating wings. Very few prototypes were built, and those that were constructed were completely unsuccessful. The essential principle is that the angle of attack of the rotating wings is altered as they go round, allowing the lift/thrust vector to be altered. This allows the aeroplane to rise vertically, hover, and even go backwards. Thus, cyclogyro-based flying robot has possibility of being a high maneuverability MAV. To the best of our knowledge, nobody has proposed effective and practical mechanism of altering angles of attack until the mechanism [8] has been proposed. Thus, there is no record of any successful flights although machines of this type have been designed by some companies. However, very recently, it was shown in [8] that the developed cyclogyro-based flying robot can generate at least enough lift force to fly.

The main purpose of this paper is to develop a more efficient and innovative flying mechanism for cyclogyro-based horizontal axis rotorcrafts. To accomplish the purpose, in this paper we propose a new pantograph-based variable wing mechanism for cyclogyro-based horizontal-axis rotorcrafts. As a first step, this paper focuses on demonstrating the possibility of the flying robot with this mechanism. Section II describes the pantograph-based variable wing mechanism and its features. In Section III we construct a simulation model of this mechanism. Section IV presents some experiments for a prototype body with the proposed pantograph-based variable wing mechanism. Both simulation and experimental results show that the flying robot with this new mechanism can generate enough lift forces to keep itself in the air. Furthermore in Section V we improve the simulation model and Section VI gives design parameters optimization using the improved simulation model. As a result of optimizing parameters we arrive at the optimal parameters of the robot that can generate lift force about 200 gf larger than its own weight.

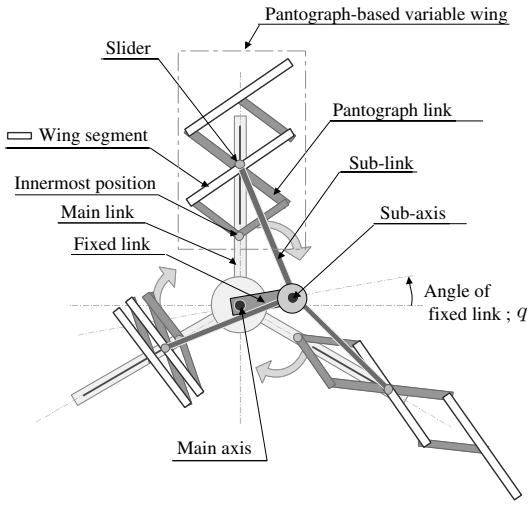

Fig. 1. Pantograph-based variable wing mechanism.

II. Pantograph-based Variable Wing Mechanism

Fig. 1 illustrates the new pantograph-based variable wing mechanism. A set of pantograph-based variable wing consists

This work was supported in part by a Grant-in-Aid for Scientific Research (C) 18560244 from the Ministry of Education, Science and Culture of Japan

N. Hara, K. Tanaka and H. Ohtake are with the Department of Mechanical Engineering and Intelligent Systems, The University of Electro-Communications, Chofu, Tokyo 182-8585, Japan (phone: +81-424-43-5425; fax: +81-424-43-5425; email: n-hara@rc.mce.uec.ac.jp; ktanaka@mce.uec.ac.jp; hohtake@rc.mce.uec.ac.jp).

H. O. Wang is with the Department of Aerospace and Mechanical Engineering, Boston University, Boston, MA 02215 USA, wangh@bu.edu

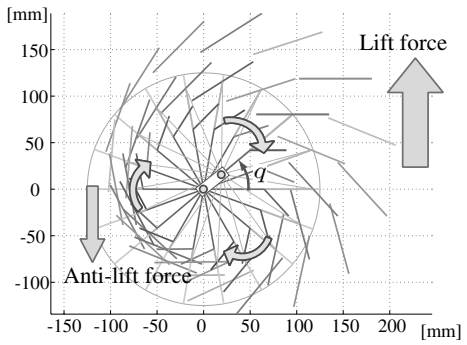

Fig. 2. Trajectory of variable wings.

TABLE I
DESIGN PARAMETERS OF PROTOTYPE BODY.

l	100 mm	e	25 mm
c	39.1 mm	b	230 mm
n_f	5 sets	n	3 seg.
Weights	245 g	γ_{max}	50 deg.

of several wing segments. This mechanism is composed of two different mechanisms, revolving slider-crank mechanism that causes revolving and reciprocating motion, and pantograph-link mechanism that causes flapping motion.

As main links rotate around the main axis, sub-links also rotate around the sub-axis due to the slider-crank mechanism. The first segment of a pantograph link is connected on the innermost position of the main link and the second segment is linked to the slider that is connected on the end of the sub-link. Thus the pantograph links expand and contract, as the sliders shuttles along the linear guides on the main link. Because of this motions, the wing segments, located on the pantograph links like as in Fig. 1, reciprocate and swing around the center of the wing chord.

Fig. 2 shows the trajectory of the wing segments according to the revolution of the main link. In downstroke motion of the wing segments, this mechanism makes motions of expanding wings and getting high attack of angles to generate heavy drags to the upward direction. Conversely in upstroke motion, this mechanism makes motions of contracting wings and getting low attack of angles to reduce anti-lift forces directing to the downward. Due to this folding up motion of the wings, it is possible for this mechanism to have a larger wing area in a small space and to get a larger lift force.

Fig. 3 shows the developed prototype body with the proposed new pantograph-based variable wing mechanism. The design parameters of this model are shown in Table I. The symbols and variables in this paper are summarized in Fig. 4. The prototype body has five sets of variable wings with three wing segments, and is totally 245 g including a 40 W brushless DC motor (about 130 g).

III. SIMULATION MODEL

This section presents a simulation model for calculating lift force of the proposed mechanism and shows the possibility of flying the robot through the developed simulation model.

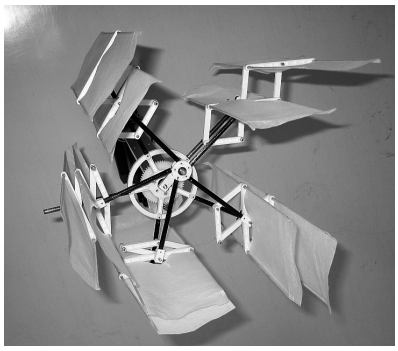

Fig. 3. Developed prototype body with pantograph-based variable wing mechanism (single unit).

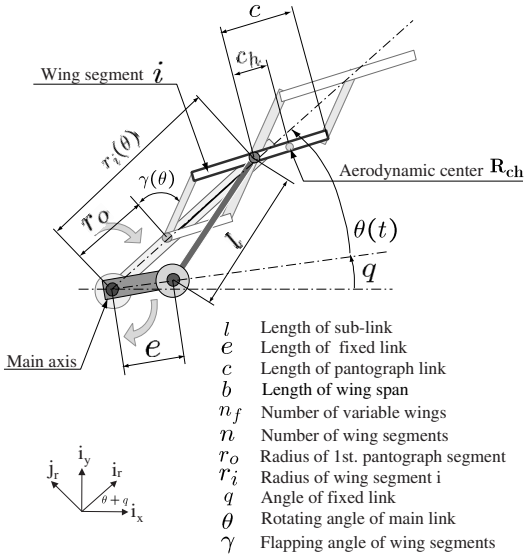

Fig. 4. Design parameters and variables in pantograph-based variable wing mechanism

A. Trajectories of wing segments

In the mechanism, the radius $r_i(\theta)$ of the wing segments i and the wing's flapping angle $\gamma(\theta)$ are functions of rotating angle $\theta(t)$ of the main axis as shown in Fig 4:

$$r_i(\theta) = r_o + (r_m(\theta) - r_o)(i-1), \quad (1)$$

$$\gamma(\theta) = cos^{-1}\frac{r_m(\theta) - r_o}{2l}, \quad (2)$$

where $r_m = ecos\theta + \sqrt{l^2 - e^2 sin^2(\theta)}$. Thus the vector $\mathbf{R}_{ch}$ from the main axis to the aerodynamic center on the wing chord (see Fig. 4) is expressed as

$$\mathbf{R}_{ch} = (r_i + csin\gamma)\mathbf{i}_r - ccos\gamma\mathbf{j}_r \quad (3)$$
$$= \begin{bmatrix} r_i + c_h sin\gamma \\ c_h cos\gamma \end{bmatrix}^T \begin{bmatrix} cos(\theta+q) & sin(\theta+q) \\ -sin(\theta+q) & cos(\theta+q) \end{bmatrix} \begin{bmatrix} \mathbf{i}_x \\ \mathbf{i}_y \end{bmatrix}.$$

B. Translational lift

This simulation considers only translational motion of the wings in the mechanism, as illustrated in Fig. 5. To consider

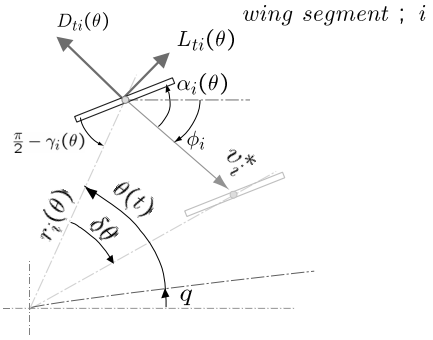

Fig. 5. Wing translation.

the translation of wing segments based on the quasi-steady theory, we need to obtain the translating velocity v^* that gives an average of dynamical pressure. In this paper, for simplicity, we fix the aerodynamic center at the 1/4 chord position $\mathbf{R}_{ch}(c_h = c/2)$. Hence for a rotational frequency $f[Hz]$ of main link, the translating velocity of wing segment i is calculated:

$$v_i^* = |\mathbf{v}_i^*| \cong \frac{2\pi f}{\delta\theta}\sqrt{\Delta R_{c_h x_i}^2 + \Delta R_{c_h y_i}^2} \quad (4)$$

$$\phi_i = \angle \mathbf{v}_i^* \cong \frac{\Delta R_{c_h y_i}}{\Delta R_{c_h x_i}} \quad (5)$$

where $\Delta\mathbf{R}_{c_h}(\theta) = (\Delta R_{c_h x}, \Delta R_{c_h y}) = \mathbf{R}_{c_h}(\theta+\delta\theta) - \mathbf{R}_{c_h}(\theta)$.

The attack angle α can be calculated as

$$\alpha_i(\theta) = -\phi_i(\theta) + \theta + q + \gamma(\theta) - \frac{\pi}{2}. \quad (6)$$

For the velocity v^*, the attack angle α, the wing segment area $S = 2cb$, and the lift/drag coefficients $C_D(\alpha)$ and $C_L(\alpha)$ shown in Fig. 6, the lift and drag of wing segment i are given by

$$D_i(\theta) = \frac{1}{2}\rho v_i^{*2}(\theta) S C_D(\alpha_i(\theta)), \quad (7)$$

$$L_i(\theta) = \frac{1}{2}\rho v_i^{*2}(\theta) S C_L(\alpha_i(\theta)). \quad (8)$$

The total torques of n_f sets with n wing segments are calculated as

$$T(\theta) = \sum_{i_f}^{n_f}\sum_{i}^{n}(D_i(\Theta_{i_f}) r_i^*(\Theta_{i_f})) + 2\pi C_{fric} f, \quad (9)$$

where

$$\Theta_{i_f} = \theta(t) + 2\pi\frac{i_f - 1}{n_f} \quad (10)$$

$$r_i^* = \frac{v_i^*}{2\pi f} = \frac{1}{\delta\theta}\sqrt{\Delta R_{c_h x_i}^2 + \Delta R_{c_h y_i}^2} \quad (11)$$

and C_{fric} is the friction loss coefficient of the prototype body given as $C_{fric} = 0.062$ mNm·sec/rad.

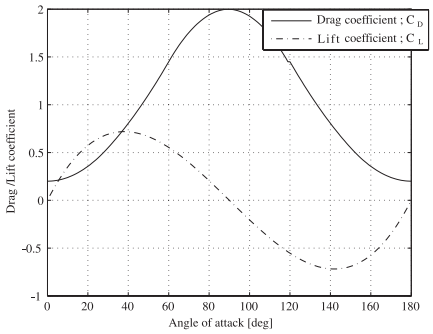

Fig. 6. Drag and lift coeficients.

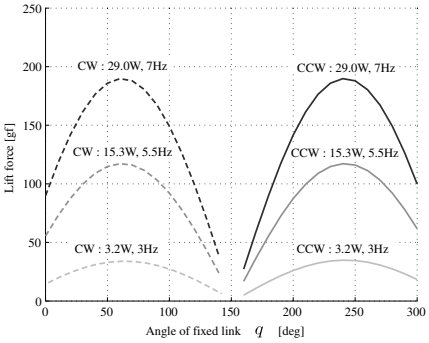

Fig. 7. Simulation results of lift forces for angle of fixed link.

The motor power P can be expressed as

$$\begin{aligned} P(\theta) &= 2\pi T(\theta) f \\ &= 4\rho\pi^3 S\sum_{i_f}^{n_f}\sum_{i}^{n}\left(r_i^{*3}(\Theta_{i_f}) C_D(\alpha_i(\Theta_{i_f}))\right) f^3 \\ &\quad + 4\pi^2 C_{fric} f^2. \end{aligned} \quad (12)$$

For given P, the rotational frequency f can be calculated by (12). Hence the lift force N directing upward is calculated as

$$N(\theta) = \rho S C_N(\theta) f^2, \quad (13)$$

$$\begin{aligned} C_N(\theta) &= 2\pi^2\sum_{i_f}^{n_f}\sum_{i}^{n}\{r_i^{*2} C_D(\alpha_i(\Theta_{i_f}))cos\Theta_{i_f} \\ &\quad + C_L(\alpha_i(\Theta_{i_f}))sin\Theta_{i_f}\}. \end{aligned} \quad (14)$$

C. Simulation results

Fig. 7 shows the simulation results for fixed link's angle q and several rotational frequencies f at each revolving direction (CW or CCW). It is found in the simulation results that the calculated lift forces are exactly the same in the CW and CCW directions and that there exists about 180 [deg.] phase difference of q.

Table II is simulation results at CCW and q=240 deg. This results show that the robot can generate nearly 330 gf lift force exceeding its own weight (245 g). This shows the possibility of flying this mechanism.

TABLE II

SIMULATION RESULTS.

q=240 deg and CCW			
Motor power P	40 W	50 W	60 W
Frequency f	7.9 Hz	8.6 Hz	9.2 Hz
Lift Force N	245 gf	290 f	331 gf

IV. EXPERIMENTS

A. Experiment system

Fig. 8 shows the experimental system for measuring lift forces. Lift forces are obtained by measuring strains of the aluminum bar with strain gages.

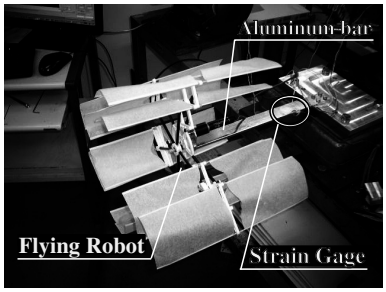

Fig. 8. Experimental system.

B. Experimental result

Fig. 9 shows the experimental result of lift forces for q at the revolving directions (CW and CCW). This result shows that in spite of the same f, the lift forces are not the same for the revolving directions. The lift forces in the CCW direction are higher than those in the CW. In addition, the required power P in the CCW are higher than that in the CW as well. However these differences do not appear in the simulation result (Fig. 7) that indicates exactly the same force distributions. We will discuss a modification of the simulation model in the next section.

In Fig. 9, the highest lift force is generated at q=210 [deg.] in the CCW direction. Fig. 10 (c) is an experimental result of lift performances shown in Fig. 10 (a) and (b) at q=210 [deg.] in the CCW direction. The lift force arrives at 330 gf that is larger than its own weight (245 gf). This means the generated lift force is sufficient to keep the robot in the air.

V. NEW SIMULATION MODEL

As a reason of the simulation error between Figs. 7 and 9, we focus on a rotational effect. The simulation model considers only translational motions. The variable wing mechanism has a very remarkable flapping motion of the pantograph. Hence the rotational motion of the wings need to be considered for this mechanism.

When a translating wing rotates, it gains Magnus-like force. As shown in Fig. 11, the Magnus-like force at highly rotating position contributes to upward in the CCW, whereas that at highly rotating position contributes to downward in the CW. In addition assuming torques by this force, torques are for the revolving directions in CW, but against the revolutions in CCW. This phenomenon can be observed in Fig. 9.

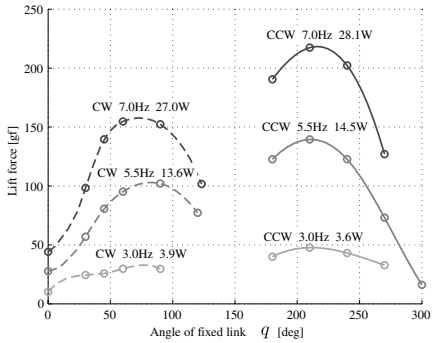

Fig. 9. Experiment results of lift forces for angle of fixed link.

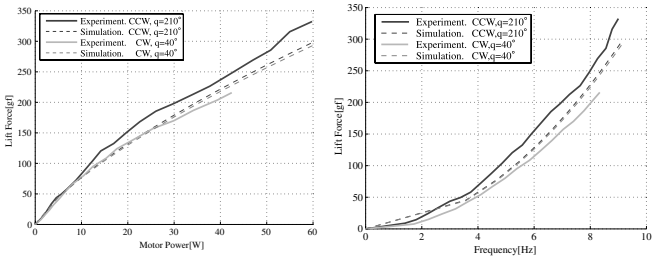

(a) (b)

Motor power P	20 W	40W	60 W
Frequency f	6 Hz	7.8 Hz	9 Hz
Lift Force N	150 gf	235 gf	330 gf

(c)

Fig. 10. Experiment result at q=210 deg in CCW. (a) Motor power P and frequency f. (b) Frequency f and lift force N. (c) Performance at each power.

In this section, we construct a new simulation model considering not only translational motions but also rotational motions.

A. Rotational lift

Fig. 12 illustrates a translating wing segment i with rotation. For the rotating velocity ω_{ri} and the translating velocity v_i^*, the leading edge velocity v_{i1} and the trailing edge velocity v_{i2} are expressed as

$$v_{i1} = v_{i1_t}\mathbf{i}_v + v_{i1_n}\mathbf{j}_v = \begin{bmatrix} |v_i^*| - c\omega_{ri}sin\alpha_i \\ c\omega_{ri}cos\alpha_i \end{bmatrix}^T \begin{bmatrix} \mathbf{i}_v \\ \mathbf{j}_v \end{bmatrix}, \quad (15)$$

$$v_{i2} = v_{i2_t}\mathbf{i}_v + v_{i2_n}\mathbf{j}_v = \begin{bmatrix} |v_i^*| + c\omega_{ri}sin\alpha_i \\ -c\omega_{ri}cos\alpha_i \end{bmatrix}^T \begin{bmatrix} \mathbf{i}_v \\ \mathbf{j}_v \end{bmatrix}. \quad (16)$$

According to conservation law of energy, pressure gradient ΔP is expressed as

$$\begin{aligned} \Delta P_i = P_{i1} - P_{i2} &= \frac{1}{2}\rho\left(|v_{i2}|^2 - |v_{i1}|^2\right) \\ &= \frac{1}{2}\rho({v_{i2}}_t^2 - {v_{i1}}_t^2) \\ &= \frac{1}{2}\rho(4c\omega_{ri}v_i^* sin\alpha_i). \end{aligned} \quad (17)$$

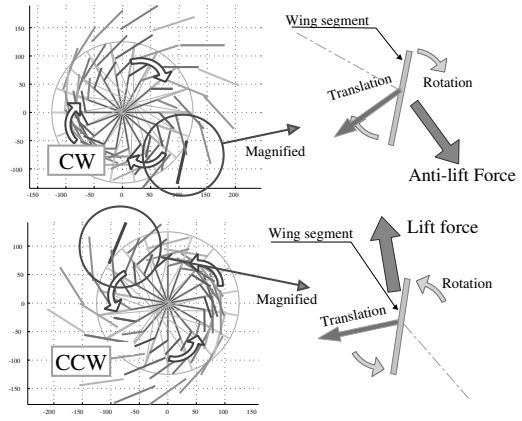

Fig. 11. Effect of rotating wing.

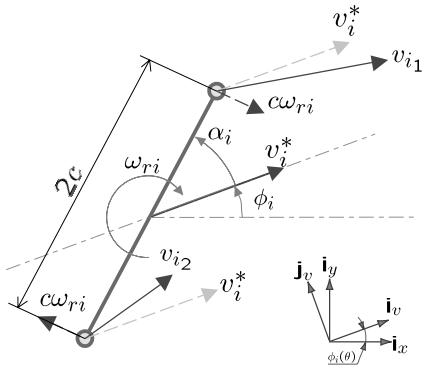

Fig. 12. Wing rotation.

This means ΔP is equal to the gradient of dynamical pressures of the wing velocity v_{i1t} and v_{i2t}. Hence assuming a flow and pressure field like water pressure illustrated in Fig. 13, the rotational lift F_{ri} of one wing segment is expressed as a pressure gradient force:

$$\begin{aligned} F_{ri} &= \begin{bmatrix} F_{ri_x} \\ F_{ri_y} \end{bmatrix} = \Delta P \cdot (2c\cos\alpha_i \cdot b) \cdot \mathbf{j}_v \\ &= \frac{1}{2}\rho(4c\omega_{ri}v_i^*\sin\alpha_i) \cdot (2c\cos\alpha_i \cdot b) \cdot \mathbf{j}_v \\ &= 4\rho c^2 b\omega_{ri}v_i^*\sin\alpha_i\cos\alpha_i \begin{bmatrix} -\sin\phi_i \\ \cos\phi_i \end{bmatrix}^T \begin{bmatrix} \mathbf{i}_x \\ \mathbf{i}_y \end{bmatrix}. \quad (18) \end{aligned}$$

Finally, the total upward force F_{ry} with respect to the rotational motion is calculated as

$$\begin{aligned} F_{ry} &= 2\rho c^2 b \sum_{i=1}^{n}\sum_{i_f=1}^{n_f}\Big(\omega_{ri}(\Theta_{i_f})v_i^*(\Theta_{i_f}) \\ &\quad \sin 2\alpha_i(\Theta_{i_f})\cos\phi_i(\Theta_{i_f})\Big). \quad (19) \end{aligned}$$

B. Simulation result of rotational lift

Fig. 14 shows simulation results of lift force distribution $N' = N + F_{ry}$ for the angle of fixed link q with considering both translational and rotational effect. The results in Fig. 14 agree well with the experimental results in Fig. 9. Fig. 15 shows lift force at each frequency (simulation and experiment). Thus, our developed simulation model considering the rotational motion has a sufficient high performance for calculating lift forces of the pantograph-based variable wing mechanism with about 10-percent error.

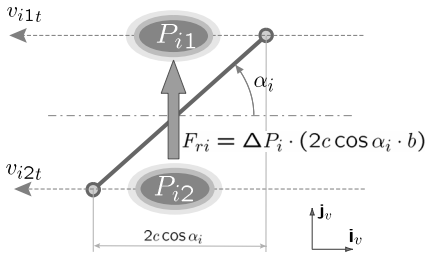

Fig. 13. Pressure gradient force F_{ri} of wing segment i.

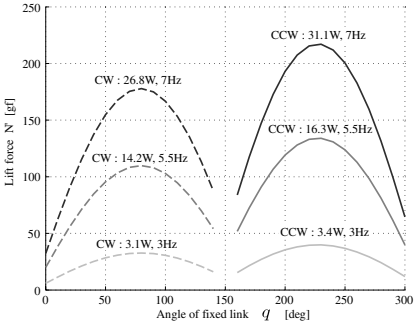

Fig. 14. Simulation results of lift force for angle of fixed link with consideration of rotational effect.

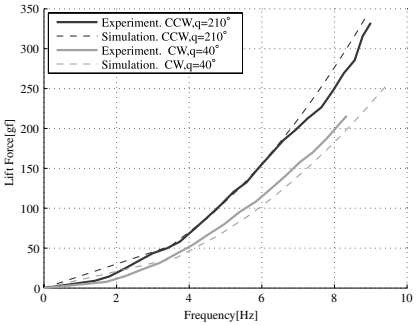

Fig. 15. Lift force at each frequency (simulation and experiment).

VI. Optimal Design Parameters

In previous section, we have showed the possibility of flying the developed prototype body. However the optimal design parameters for the prototype body have not been considered. This section provides some optimization results for the design parameters of the prototype body through the simulation model developed in Section V.

A. Performance function of gaining lift

The purpose of the optimization is to determine the design parameters that can generate larger payload. To evaluate the

TABLE III

RANGES OF DESIGN PARAMETERS.

l	80 $\sim$ 140 mm	e	0 $\sim$ 70 mm
n_f	3 $\sim$ 6 sets	c	0 $\sim$ 100 mm
n	2 $\sim$ 4 seg.	b	280 mm
γ_{max}	$50deg$		

payload in the simulation model, we need to formulate a weight model $M[g]$ of the developed prototype body for changing the design parameters. By considering the specific gravity and sizes of materials, the weight model is formulated as

$$\begin{aligned} M &= 160 + 0.135(10 + e) + 2.4n_f \\ &\quad +0.015(e + l - r_o + 30 + l)n_f \\ &\quad +5.7 \times 10^{-5}(r_o - 20)^2 + 1.04 \times 10^{-5}(4n - 3)n_f c^3 \\ &\quad +22S + 1.15 \times 10^{-7} b^3 (n - 1)n_f \end{aligned} \quad (20)$$

where the first term is the weight of motor and all unchanging structural parts, the second term is of fixed link, the third term is of sliders, the forth term is of cranks, the fifth term is of gears, the sixth term is of pantograph links, and the last two terms are of wings.

Table III shows the searching area in design parameter optimization. We search the optimal parameter by calculating the payload $P_L(= N' - M)$ for all combinations of variable parameters. In this paper we optimize the five parameters l, e, n_f, c, and n.

B. Optimization result

Tables IV and V show optimization results for P=40 [W] and 60 [W], respectively. Comparing these results, the optimal parameters are dependent of the motor power P. Small wing areas are selected at low power, whereas large wing areas are selected at high power. This shows that the optimal parameters are obviously a function of motor power P. Hence we have to keep in mind to design properly for machines scale and motor output. It seems that the developed prototype body is improper to the $40 \sim 60$ [W] motor scale, and it could be well-suited to lower power around $10 \sim 20W$.

Comparing the searched optimal body with the developed prototype body both in 40 [W] and 60 [W], the optimal bodies are supposed to generate higher payload. In particular at 60 [W], the optimal body B' can be expected to get over 200 gf payloads although the payload of the prototype body is 107 gf. This result shows the possibility of great progress in lift generation performances of this mechanism.

VII. CONCLUSIONS

We proposed a pantograph-based variable wing mechanism, and developed a simulation model considering both the translational and rotational motions. The simulation model agrees well with experimental results. The developed prototype body generates about 330 gf lift force for its own weight (245 g). As a result of the design parameter optimization through the simulation model, we arrived at the optimal parameter with 210 gf payloads. Thus, we demonstrated the possibility of flying through computer simulations and experiments.

One of our next subjects is to develop a flying robot with the optimal parameters and to evaluate its flying performance in experiments.

TABLE IV

OPTIMIZED DESIGN PARAMETERS I (40 W).

	n	n_f	l	e	c	S	$Payload$	$freq.$
	seg.	set	mm	mm	mm	m^2	gf	Hz
A	3	2	120	60	85	0.15	67	7.2
B	3	3	90	40	60	0.21	86	6.7
C	3	4	90	35	55	0.29	81	5.2
D	4	3	110	35	55	0.25	67	6.0
E	5	3	110	30	45	0.26	55	6.4
Prototype	5	3	100	25	40	0.18	16	7.7

TABLE V

OPTIMIZED DESIGN PARAMETERS II (60 W).

	n	n_f	l	e	c	S	$Payload$	$freq.$
	seg.	set	mm	mm	mm	m^2	gf	Hz
A'	3	2	130	65	90	0.16	178	7.7
B'	3	3	100	50	70	0.24	210	6.6
C'	3	4	90	40	60	0.31	162	8.2
D'	4	3	130	50	70	0.32	184	5.3
E'	5	3	110	30	45	0.26	165	7.4
Prototype	5	3	100	25	40	0.18	107	8.9

REFERENCES

[1] Fritz-Olaf Lehmann, *The mechanisms of lift enhancement in insect flight*, Naturwissenschaften, vol.91, No.3, pp.101-122, 2004.

[2] M. H. Dickinson, F. O. Lehmann and S. P. Sane, *Wing Rotation and the Aerodynamic Basis of Insect Flight*, Science, 284:1954-60, June 1999.

[3] J. Yan, S.A. Avadhanula, J. Birch, M.H. Dickinson, *Wing Transmission for a Micromechanical Flying Insect*, IEEE/ICRA, Vol.2, pp.1509-1516 (2000).

[4] J. M. Grasmeyer and M. T. Keennon, Development of the black widow micro air vehicle, AIAA-2001-0127, pp.1-9 (2001).

[5] S.M. Ettinger, M.C. Nechyba, P.G. Ifju, and M. Waszak, Vision-guided flight stability and control for micro air vehicles, Advanced Robotics, Vol.17, No.3, pp.617-640 (2003).

[6] T. Hase, *A cyclogyro-based flying robot*, SVBL conference in UEC, P-12, 2001

[7] T. Hase, T. Suzuki, K. Tanaka, T. Emaru, *A Flying Robot with Variable Attack Angle Mechanism*, The 21st Annual Conference of the Robotics Society of Japan, 3B22, in CD (2003)

[8] Y. Higashi, K. Tanaka, T. Emaru, and H. O. Wang, *Developement of a Cyclogyro-based Flying Robot with Variable Attack Angle Mechanisms*, 2006 IEEE/RSJ International Conference on Intelligent Robotics and Systems, Beijing, 2006 ,pp. 3261-3266.

[9] The Cyclogyros:Planned paddle-wheel aeroplanes, http://www.dself.dsl.pipex.com/MUSEUM/TRANSPORT/cyclogyro/cyclogyro.htm